Computers and Mathematics with Applications 61 (2011) 3606–3617

Contents lists available at ScienceDirect

Computers and Mathematics with Applications

journal homepage: www.elsevier.com/locate/camwa

Evaluation of three lattice Boltzmann models for multiphase flows in porous media

Haibo Huang*, Lei Wang, Xi-yun Lu

Department of Modern Mechanics, University of Science and Technology of China, Hefei, 230026, China

ARTICLE INFO

Article history:
Received 21 October 2009
Received in revised form 14 June 2010
Accepted 22 June 2010

Keywords:
Lattice Boltzmann
Multiphase
Shan–Chen
Free energy
Multicomponent
Porous media

ABSTRACT

A free energy (FE) model, the Shan–Chen (S–C) model, and the Rothman and Keller (R–K) model are studied numerically to evaluate their performance in modeling two-dimensional (2D) immiscible two-phase flow in porous media on the pore scale. The FE model is proved to satisfy the Galilean invariance through a numerical test and the mass conservation of each component in the simulations is exact. Two-phase layered flow in a channel with different viscosity ratios was simulated. Comparing with analytical solutions, we see that the FE model and the R–K model can give very accurate results for flows with large viscosity ratios. In terms of accuracy and stability, the FE model and the R–K model are much better than the S–C model. Co-current and countercurrent two-phase flows in complex homogeneous media were simulated and the relative permeabilities were obtained. Again, it is found that the FE model is as good as the R–K model in terms of accuracy and efficiency. The FE model is shown to be a good tool for the study of two-phase flows with high viscosity ratios in porous media.

1. Introduction

1.1. The lattice Boltzmann model for multiphase flow

The lattice Boltzmann method (LBM) is based on mesoscopic kinetic equations [1]. Comparing with the conventional methods for multiphase flows, the LBM does not track interfaces, while sharp interfaces can be maintained automatically [2]. LBM has also been successfully applied to study multiphase phenomena, for example the wetting and spreading of two fluids [3–9] and multiphase flow in porous media [10–12].

There are several popular multiphase LBM models. The first one is the color-gradient model proposed by Gunstensen et al. [13] which is based on the Rothman–Keller (R–K) lattice gas model [14]. Grunau et al. [15] modified the model to handle binary fluids with different density and viscosity ratios. Recently, Ahrenholz et al. improved the R–K model [16] and used a multiple-relaxation-time LB model to handle cases of higher viscosity ratios and lower capillary numbers. The advantage of the R–K model is that the surface tension and the ratios of densities and viscosities can be adjusted independently [16].

The second one is the Shan–Chen (S–C) model [17]. The S–C single-component multiphase model works well with high density ratios [18], but the surface tension and the ratios of densities and viscosities cannot be adjusted independently. Some parameters have to be determined through numerical experiments [16]. Pan et al. [10] and Li et al. [11] applied the S–C two-component model to study the two-component flow in porous media. The maximum viscosity ratio in their study is about 3 due to numerical instability [11].

* Corresponding author.
E-mail address: huanghb@ustc.edu.cn (H. Huang).

0898-1221/$ – see front matter © 2010 Elsevier Ltd. All rights reserved.
doi:10.1016/j.camwa.2010.06.034

The third one is the free energy (FE) LBM [19]. However, the original FE model [19] does not have Galilean invariance for the viscous terms in the Navier–Stokes equation [1,19]. Inamuro et al. [2] achieved a high density ratio through improving Swift's free energy model [19], but using the model involves solving a Poisson equation, which decreased the simplicity of the usual LBM. Zheng et al. proposed a Galilean invariant FE LB model [20]. This model is simpler than that of Inamuro et al. Here we will evaluate the model as regards modeling multiphase flow in porous media.

There are some theoretical analyses [1,19] of these three models but very few studies are based on numerical analysis [21]. In Ref. [21], Hou et al. compared the S–C and the R–K models and focused on drop/bubble simulation. However, there are no strict quantitative comparisons with other available analytical solutions.

Here we evaluate three models: the R–K model [13–15], the S–C model [17], and the FE model [19] and mainly focus on the FE model. Some other multiphase LB models [22,23] are not evaluated here.

The density ratio between two components may be concerned in some situations. The S–C single-component multiphase model is able to mimic flows with large density ratio [18]. However, if the S–C multicomponent model is used, the density ratio is around unity. The R–K model seems able to simulate flows with large density ratio [15,16]. However, we found that for layered two-phase flow through a 2D channel, quantitative comparisons between the result obtained from the R–K model and the analytical solution are not good when the density ratio is not unity. If the density ratio is large, the discrepancy between the R–K result and the analytical solution becomes large. For the FE model, Zheng et al. [20] claimed that the model is able to mimic flows with large density ratio. However, Fakhari and Rahimian [24] recently found that this is not true and the model seems only suitable for a density-matched binary fluid.

Our numerical study is limited to two-dimensional (2D) simulations and the density ratio in all cases is around unity. We first briefly review the three multiphase models. Then the accuracy of these models is examined by comparing the numerical solution with the analytical solution for layered two-phase flow through a 2D channel. After that, multiphase flow in homogeneous porous media with different wettabilities is simulated and analyzed.

1.2. Two-phase flow in porous media

The isotropic flow of a Newtonian fluid through a porous medium can be described by Darcy's law $\mathbf{u} = -\frac{k\mathbf{G}}{\mu}$, where $\mathbf{u}$ is the average velocity of the fluid in the direction of a pressure gradient, $\mathbf{G}$ is the driving force per unit volume or the pressure gradient, and μ is the viscosity of the fluid. k is the permeability in the direction of $\mathbf{G}$. It measures the ability of a porous medium to transmit fluids in a specified direction.

For multiphase flows in porous media, momentum transfer may occur between the two fluids, which is called the viscous coupling effect [25]. To account for the viscous coupling effects, usually four dimensionless relative-permeability parameters k_{ij} are used to measure the effective permeability of two-phase flow in two dimensions. They are defined by modifying Darcy's law as in [26]: $\mathbf{u}_i = -\sum_{j=1}^{2} \frac{kk_{ij}\mathbf{G}_j}{\mu_j}$, where i, j indicate phase 1 or 2, and $\mathbf{u}_i$ is the average velocity of fluid phase i. The relative permeabilities k_{ij} are usually functions of the wetting saturation S_w, the capillary number Ca and the viscosity ratio M. S_w means the volumetric fraction of the wetting phase contained in pores. $Ca = \frac{u_w\mu_w}{\sigma}$ is the capillary number, where u_w is the average velocity of the wetting phase, and σ is the surface tension. M is defined as $M = \frac{\mu_{nw}}{\mu_w}$, which means the dynamic viscosity ratio between the nonwetting and the wetting fluids.

To determine k_{ij}, two numerical simulations can be carried out [12]. For one simulation, driving forces are applied in the same direction, i.e., $\mathbf{G}_1 = \mathbf{G}_2$ (co-current flow), while for the other simulation, the driving forces are in opposite directions, i.e., $\mathbf{G}_1 = -\mathbf{G}_2$ (countercurrent flow).

In this paper we evaluate the performance of the three different models in the study of two-phase flow in a homogeneous porous medium. Although particular models have been applied to study oil–water displacement in porous media [10–12, 16,27,28], to the best of our knowledge, detailed numerical comparison of the efficiency and accuracy of the three models has not been reported for two-phase flow in porous media. For simplicity, in all of our numerical simulations, the two fluids may have different viscosities but have the same density.

2. Method

2.1. The FE model

The FE model improved by Zheng et al. [20] is introduced briefly in this section. In the model, two lattice Boltzmann equations are used to solve the 2D Navier–Stokes equations and a Cahn–Hilliard equation, i.e., Eq. (1), which are used to describe 2D immiscible two-phase flows [29–31]:

$$\partial_t \phi + \partial_\beta \left(\phi u_\beta\right) = \theta_M \partial_\beta \left(\partial_\beta \mu_\phi\right). \tag{1}$$

The subscripts $\alpha, \beta, \ldots$ will be used to represent Cartesian coordinates and ∂_t, ∂_α denote differentiation with respect to t and x_α, respectively. Summation over repeated indices is assumed. In the above equations, μ_ϕ is the chemical potential, and θ_M is the mobility, which is a constant in our study. $\phi(\mathbf{x}, t) = \rho_1(\mathbf{x}, t) - \rho_2(\mathbf{x}, t)$ is an order parameter and changes between -1 and 1. $\rho(\mathbf{x}, t) = \rho_1(\mathbf{x}, t) + \rho_2(\mathbf{x}, t)$ is the density of the fluid at position $(\mathbf{x}, t)$.

In this FE model [20,32], to solve the 2D Navier–Stokes equation, a common lattice Boltzmann equation (LBE) is employed:

$$f_i(\mathbf{x}+\mathbf{e}_i\delta t, t+\delta t) - f_i(\mathbf{x}, t) = \frac{1}{\tau_\rho}\left[f_i^{\mathrm{eq}}(\mathbf{x}, t) - f_i(\mathbf{x}, t)\right] + S_i, \tag{2}$$

where $f_i(\mathbf{x}, t)$ is the density distribution function in the ith velocity direction. S_i is a source term added into the LBE to mimic the body force term that appears in the Navier–Stokes equation. To make the relaxation parameter change smoothly at the interfaces between two fluids, the relaxation time τ_ρ is chosen as $\tau_\rho = \left(\nu_1^{\frac{\rho+\phi}{2\rho}}\nu_2^{\frac{\rho-\phi}{2\rho}}/c_s^2\right)\delta t + 0.5$ [33], where ν_1 and ν_2 are the kinematic viscosities of fluids 1 and 2, respectively.

In the above equation, the $\mathbf{e}_i$s are the discrete velocities. For the D2Q9 model, they are given by

$$[\mathbf{e}_0, \mathbf{e}_1, \mathbf{e}_2, \mathbf{e}_3, \mathbf{e}_4, \mathbf{e}_5, \mathbf{e}_6, \mathbf{e}_7, \mathbf{e}_8] = c\cdot\begin{bmatrix}0 & 1 & 0 & -1 & 0 & 1 & -1 & -1 & 1\\ 0 & 0 & 1 & 0 & -1 & 1 & 1 & -1 & -1\end{bmatrix},$$

where $c = \frac{\delta x}{\delta t}$ is the ratio of lattice spacing δx and time step δt. Here, we define one lattice unit (δx) as 1 lu and one time step (δt) as 1 ts.

Here the body force term appearing in the above Navier–Stokes equation is $F_\alpha + \mu_\phi\partial_\alpha\phi$, where μ_ϕ is the chemical potential, can be derived from the free energy density function in the following section. The source term can take the following form:

$$S_i = \frac{e_{i\alpha}\omega_i}{c_s^2}\left(F_\alpha + \mu_\phi\partial_\alpha\phi\right). \tag{3}$$

To recover the NS equations through Chapman–Enskog expansion, the equilibrium distribution functions f_i^{eq} are constructed as follows [20]:

$$f_i^{\mathrm{eq}} = \omega_i A_i + \omega_i\rho\left(\frac{e_{i\alpha}u_\alpha}{c_s^2} + \frac{e_{i\alpha}u_\alpha e_{i\beta}u_\beta}{2c_s^4} - \frac{u_\alpha u_\alpha}{2c_s^2}\right), \tag{4}$$

where $w_i = 4/9$ $(i=0)$, $w_i = 1/9$ $(i=1,2,3,4)$, $w_i = 1/36$ $(i=5,6,7,8)$, $c_s = \frac{c}{\sqrt{3}}$. The other coefficients are chosen as [20]

$$\begin{aligned} A_0 &= \frac{9}{4}\rho - \frac{15}{4}\left(\phi\mu_\phi + c_s^2\rho\right),\\ A_i &= 3\left(\phi\mu_\phi + c_s^2\rho\right), \quad i = 1, 2, \ldots, 8.\end{aligned} \tag{5}$$

The macrovariables can be obtained from $\rho = \sum_i f_i$ and $\rho\mathbf{u} = \sum_i f_i\mathbf{e}_i$.

The Cahn–Hilliard equation, i.e., the interface-capturing equation, can be solved by using a LBE with a set of D2Q5 distribution functions g_i [32]. The D2Q5 model is simpler than the D2Q9 model and able to save memory used in simulations. Here, the following slightly modified LBE is adopted [20,34]:

$$g_i(\mathbf{x}+\mathbf{e}_i\delta t, t+\delta t) - g_i(\mathbf{x}, t) = (1-q)\left[g_i(\mathbf{x}+\mathbf{e}_i\delta t, t) - g_i(\mathbf{x}, t)\right] + \frac{1}{\tau_\phi}\left[g_i^{\mathrm{eq}}(\mathbf{x}, t) - g_i(\mathbf{x}, t)\right], \tag{6}$$

where τ_ϕ is a dimensionless single relaxation time which is different from the parameter τ_ρ, and q is a constant. If q is set to 1, the above Eq. (6) is the conventional LBE. In the equation, the lattice velocities are $\mathbf{e}_0 = c\cdot(0,0)$, $\mathbf{e}_1 = c\cdot(1,0)$, $\mathbf{e}_2 = c\cdot(0,1)$, $\mathbf{e}_3 = c\cdot(-1,0)$, $\mathbf{e}_4 = c\cdot(0,-1)$.

The macroscopic variables are evaluated using $\phi = \sum_i g_i$.

Applying the Chapman–Enskog expansion and the Taylor expansion [35] to Eq. (6) and retaining terms to $O(\delta t^2)$, we can obtain the Cahn–Hilliard equation if the parameters q and mobility θ_M are chosen as $q = \frac{1}{\tau_\phi+0.5}$ and $\theta_M = -\left(\frac{q}{2} - \tau_\phi q^2\right)\delta t\Gamma$.

The equilibrium distribution function is taken as the following form [20]:

$$g_i^{\mathrm{eq}} = A_i + B_i\phi + C_i\phi e_{i\alpha}u_\alpha. \tag{7}$$

The coefficients can be chosen as $B_0 = 1$, $B_i = 0$ $(i\neq 0)$, $C_i = \frac{1}{2q}$, $A_0 = -3\Gamma\mu_\phi$, $A_i = \frac{1}{2}\Gamma\mu_\phi$, where Γ is used to control the mobility. τ_ϕ is usually chosen as 0.7 in our simulations.

This FE model requires the following interface modeling. In the Navier–Stokes equations, the term $\partial_\alpha(p_{\alpha\beta})$ is related to the surface tension force. This term can be written as a potential term [30,36] $\partial_\alpha(p_{\alpha\beta}) = -\phi\partial_\alpha\mu_\phi - \partial_\alpha p_0$, where $p_0 = \rho c_s^2$.

We adopt a free energy function in a closed volume with a mixture of two fluids in the form [30,37]

$$F = \int \Psi\,\mathrm{d}V = \int \mathrm{d}V\left[a\left(\phi^2 - \phi^{*2}\right)^2 + \frac{k_s}{2}(\partial_\alpha\phi)^2 + \frac{\rho\ln\rho}{3}\right]. \tag{8}$$

Here, V is a control volume, k_s is a coefficient that is related to the surface tension and the thickness of the interface layer. a is an amplitude parameter for controlling the energy of interaction between the two phases. This form will contribute to two equilibrium states, ϕ^* and $-\phi^*$. The chemical potential is [30]

$$\mu_\phi = a\left(4\phi^3 - 4\phi^{*2}\phi\right) - k_s\partial_\alpha^2\phi. \tag{9}$$

The pressure tensor is [30]

$$p_{\alpha\beta} = p\delta_{\alpha\beta} - k_s\left[\left(\partial_\alpha\phi\right)^2\delta_{\alpha\beta} - \partial_\alpha\phi\partial_\beta\phi\right], \tag{10}$$

where $p = a\left(3\phi^4 - 2\phi^{*2}\phi^2 - \phi^{*4}\right) - k_s\phi\partial_\alpha^2\phi + \frac{k_s}{2}\left(\partial_\alpha\phi\right)^2 + \frac{\rho}{3}$.

It should be noted there are some first and second derivatives in the above equations and they can be evaluated through finite difference schemes, i.e., $\frac{\partial\phi}{\partial x_\alpha} = \sum_{i=1}^{8}\frac{\omega_i e_{i\alpha}\cdot\phi(\mathbf{x}+e_{i\alpha}\delta t)}{c_s^2\delta t}$, $\partial_\alpha^2\phi = 2\cdot\sum_{i=1}^{8}\frac{\omega_i[\phi(\mathbf{x}+\mathbf{e}_i\delta t)-\phi(\mathbf{x})]}{c_s^2(\delta t)^2}$, where the ω_i are defined later in Eq. (4).

Following the same procedure as Refs. [29,30], we can obtain the order parameter profile along the normal direction of the interface $\phi = \phi^*\tanh(2\zeta/W)$, where ζ is the coordinate which is perpendicular to the interface, and W is the thickness of the interface layer [30]:

$$W = \frac{\sqrt{2k_s/a}}{\phi^*}. \tag{11}$$

For a flat interface, the surface tension coefficient can be evaluated as [37] $\sigma = \int k_s\left(\frac{\partial\phi}{\partial\zeta}\right)^2 \mathrm{d}\zeta$. Hence, the surface tension coefficient is

$$\sigma = \frac{4aW}{3}\phi^{*4}, \tag{12}$$

where in our simulations, $\phi^* = 1$ and the interface thickness is usually specified as larger than four lattice units [20]. The surface tension σ should be specified in simulations and then the parameter a is fully determined through Eq. (12).

2.2. The S–C multicomponent model

Here we implement the 2D S–C model [17] for a multicomponent system. In the model, one distribution function is introduced for each of the two fluid components. Each distribution function represents a fluid component and satisfies the following lattice Boltzmann equation:

$$f_i^\sigma(\mathbf{x}+\mathbf{e}_i\delta t, t+\delta t) = f_i^\sigma(\mathbf{x}, t) - \frac{\delta t}{\tau_\sigma}\left(f_i^\sigma(\mathbf{x}, t) - f_i^{\sigma,\mathrm{eq}}(\mathbf{x}, t)\right), \tag{13}$$

where $f_i^\sigma(\mathbf{x}, t)$ is the σth-component density distribution function in the ith velocity direction and τ_σ is a relaxation time which is related to the kinematic viscosity as $\nu_\sigma = c_s^2(\tau_\sigma - 0.5\delta t)$. The equilibrium distribution function $f_i^{\sigma,\mathrm{eq}}(\mathbf{x}, t)$ can be calculated as

$$f_i^{\sigma,\mathrm{eq}}(\mathbf{x}, t) = w_i\rho_\sigma\left[1 + \frac{\mathbf{e}_i\cdot\mathbf{u}_\sigma^{\mathrm{eq}}}{c_s^2} + \frac{(\mathbf{e}_i\cdot\mathbf{u}_\sigma^{\mathrm{eq}})^2}{2c_s^4} - \frac{(\mathbf{u}_\sigma^{\mathrm{eq}})^2}{2c_s^2}\right] \tag{14}$$

where ρ_σ is the density of the σth component, which can be obtained from $\rho_\sigma = \sum_i f_i^\sigma$.

The macroscopic velocity $\mathbf{u}_\sigma^{\mathrm{eq}}$ is given by

$$\mathbf{u}_\sigma^{\mathrm{eq}} = \mathbf{u}' + \frac{\tau_\sigma\mathbf{F}_\sigma}{\rho_\sigma}, \tag{15}$$

where $\mathbf{u}'$ is a velocity common to the various components defined as

$$\mathbf{u}' = \frac{\sum_\sigma\left(\sum_i\frac{f_i^\sigma\mathbf{e}_i}{\tau_\sigma}\right)}{\left(\sum_\sigma\frac{\rho_\sigma}{\tau_\sigma}\right)}. \tag{16}$$

In Eq. (15), $\mathbf{F}_\sigma = \mathbf{F}_{c,\sigma} + \mathbf{F}_{\mathrm{ads},\sigma}$ is the force acting on the σth component, here including the fluid–fluid cohesion $\mathbf{F}_{c,\sigma}$, and fluid–solid adhesion $\mathbf{F}_{\mathrm{ads},\sigma}$.

Each node in the computational domain is occupied by every σth component, though one is dominant under most conditions as described below. The minor components can be thought of as dissolved within the dominant component.

With the techniques used here, the overall density of fluid in the domain is approximately uniform because the densities are complementary in the sense that $\sum_\sigma \rho_\sigma = \rho$ (the constant initial density) in a two-fluid system.

The cohesive force acting on the σth component is defined as [27]

$$\mathbf{F}_{c,\sigma}(\mathbf{x}, t) = -G_c \rho_\sigma(\mathbf{x}, t) \sum_i w_i \rho_{\bar\sigma}(\mathbf{x} + \mathbf{e}_i \delta t, t)\mathbf{e}_i, \tag{17}$$

where the σ and $\bar\sigma$ denote two different fluid components and G_c is a parameter that controls the strength of the cohesion force.

The surface force acting on the σth component can be computed as follows [27]:

$$\mathbf{F}_{\text{ads},\sigma}(\mathbf{x}, t) = -G_{\text{ads},\sigma} \rho_\sigma(\mathbf{x}, t) \sum_i w_i s(\mathbf{x} + \mathbf{e}_i \delta t)\mathbf{e}_i. \tag{18}$$

Here $s(\mathbf{x} + \mathbf{e}_i\delta t)$ is an indicator function that is equal to 1 or 0 for a solid or a fluid domain node, respectively. The strength of interaction between each fluid and a wall can be adjusted using the parameters $G_{\text{ads},\sigma}$. Most previous literature has suggested that $G_{\text{ads},\sigma}$ should be positive for nonwetting fluid and negative for wetting fluid [5,10,27].

2.3. The R–K model

In the R–K model, for convenience, three distribution functions are defined here: f_i, f_i^σ or f_i^{red}, $f_i^{\bar\sigma}$ or f_i^{blue}, and $f_i = f_i^\sigma + f_i^{\bar\sigma}$. Hence, the superscripts σ and $\bar\sigma$ can also be referred to as indicating the "red" and "blue" components.

The post-collision distribution function f_i^+ is [8]

$$f_i^+(\mathbf{x}, t) = f_i(\mathbf{x}, t) + (\Omega_i)^1 + (\Omega_i)^2, \tag{19}$$

where there are two collision terms in the equation.

The first collision term is $(\Omega_i)^1 = -\frac{\delta t}{\tau}\left(f_i(\mathbf{x}, t) - f_i^{\text{eq}}(\mathbf{x}, t)\right)$, and the second collision term is $(\Omega_i)^2 = A|\mathbf{f}|(2\cdot\cos^2(\lambda_i) - 1)$.

The f_i^{eq} have the same form as Eq. (14), but the ρ_σ should be replaced by ρ, which is $\rho = \rho_\sigma + \rho_{\bar\sigma}$. λ_i is the angle between the color gradient $\mathbf{f}$ and the direction $\mathbf{e}_i$; hence $\cos(\lambda_i) = \frac{\mathbf{e}_i\cdot\mathbf{f}}{|\mathbf{e}_i|\cdot|\mathbf{f}|}$ [8].

The color gradient $\mathbf{f}(\mathbf{x}, t)$ is calculated as [8]

$$\mathbf{f}(\mathbf{x}, t) = \sum_i \mathbf{e}_i \sum_j [f_j^\sigma(\mathbf{x} + \mathbf{e}_i\delta t, t) - f_j^{\bar\sigma}(\mathbf{x} + \mathbf{e}_i\delta t, t)]. \tag{20}$$

Then the recoloring step is implemented to achieve separation of the two fluids [8]:

$$f_i^{\sigma,+} = \frac{\rho_\sigma}{\rho} f_i^+ + \beta \cdot \frac{\rho_\sigma \rho_{\bar\sigma}}{\rho^2} f_i^{(\text{eq})}(\rho, 0)\cos(\lambda_i). \tag{21}$$

$$f_i^{\bar\sigma,+} = \frac{\rho_{\bar\sigma}}{\rho} f_i^+ - \beta \cdot \frac{\rho_\sigma \rho_{\bar\sigma}}{\rho^2} f_i^{(\text{eq})}(\rho, 0)\cos(\lambda_i). \tag{22}$$

After $f_i^\sigma(\mathbf{x}, t)$ and $f_i^{\bar\sigma}(\mathbf{x}, t)$ are updated, the streaming steps should be implemented for each component. That is, $f_i^\sigma(\mathbf{x} + \mathbf{e}_i\delta t, t + \delta t) = f_i^{\sigma,+}(\mathbf{x}, t)$. Through iteration of the procedure illustrated above, two-phase flow can be simulated.

In the model, A, and β are the two most important parameters that adjust interface properties. The interface thickness can be adjusted by using β and the surface tension is determined only by A [8]. To make the relaxation parameter change smoothly at the interfaces between two fluids, we also adopt the scheme constructed by Grunau et al. [15].

3. Results and discussion

3.1. Galilean invariance and the contact angle

It is well known that the previous FE model had the deficiency that it lacked Galilean invariance [19]. The S–C model [17] and the R–K model [13–15] do not have such a deficiency. Here we will firstly demonstrate that the present FE model is able to satisfy the Galilean invariance principle. A moving circular bubble was simulated as the cases in Ref. [38]. The computational domain is 100×100 and the characteristic length is $L = 100$ (δx). A circular bubble with a radius of 25 (δx) is put at the center of the domain and brought to the equilibrium state after 20,000 ts. Then the top and bottom boundary begin to move with a constant velocity $u_w = 0.01$ at $t = 0$. The periodic boundary condition is applied to the left and right boundaries. The bubble shape and velocity vectors in the computational domain are shown in Fig. 1. From the figure, we can see that the bubble becomes a circle again when the nondimensional time is $tu_w/L = 3.6$. The simulation was run for 500,000 ts and the bubble is found to keep the circle shape after $tu_w/L = 3.6$. Hence, Galilean invariance can be satisfied in this FE model.

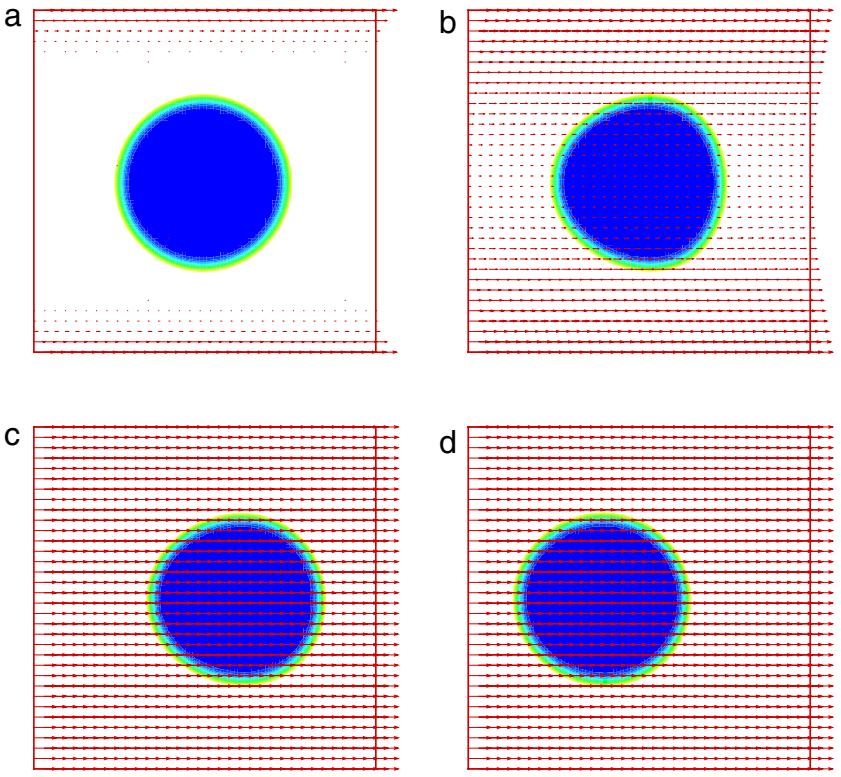

Fig. 1. Velocity vectors and density contours of a moving bubble. The computational domain is 100×100 lu^2. The relaxation parameters for the blue (gray) and white phases are $\tau_1 = 0.6$ and $\tau_2 = 1.0$, respectively. (a) $tu_w/L = 0.005$; (b) $tu_w/L = 0.2$; (c) $tu_w/L = 2.8$; (d) $tu_w/L = 3.6$. (For interpretation of the references to colour in this figure legend, the reader is referred to the web version of this article.)

The contact angle is an important issue when evaluating these multiphase models. In the S–C model, to specify a contact angle for two equal-viscosity components, we can adjust the parameters G_{ads1} and G_{ads2} [7]. If the two components have different viscosities, the contact angle can also approximately determined from (8) in Ref. [7].

In the R–K model, the contact angle can be adjusted by changing the total density ρ in the wall boundary [8].

To specify a contact angle in the FE model, a surface energy $\varphi(\phi_s)$ for solid nodes should be added into the free energy calculation (i.e., Eq. (8)). The $\varphi(\phi_s)$ is assumed to be a simple linear function of the ϕ value for the solid nodes [39], i.e., $\varphi(\phi_s) = -\omega\phi_s$. A natural boundary condition for the ϕ is [39]

$$\mathbf{n} \cdot (\nabla\phi)_s = \frac{-\omega}{k_s}, \tag{23}$$

where $\mathbf{n}$ is the local normal direction of the wall pointing into the fluid and ω is a parameter related to the surface wetting property.

The contact angle measured in fluid with $\phi = -1$ is [39]

$$\cos\theta = \frac{1}{2}\left[\left(\sqrt{1-\tilde{\omega}}\right)^3 - \left(\sqrt{1+\tilde{\omega}}\right)^3\right], \tag{24}$$

where $\tilde{\omega} = \omega/\left(\sqrt{2k_s a}\right)$. For a desired contact angle θ, the ω can be obtained according to Eq. (24). Hence, for the first-order partial derivatives, one of the derivatives is known from Eq. (23) and the other one can be obtained through a central difference scheme. For the $\nabla^2\phi$ used in the LBM, we can hybridize the biased and central difference schemes to calculate the value [32].

Applying the above boundary condition, one can obtain different contact angles as illustrated in Fig. 2 through changing the parameter ω. In the simulations, the initial shapes of the "blue" (or "gray") phase (with $\phi = -1$) are half-circles attached the wall and the final steady states are shown in the figure. From the figure, we can see that the actual contact angles agree well with the theoretical ones calculated from Eq. (24) with the parameters listed in the caption of the figure.

3.2. Layered two-phase flow in a 2D channel

Here we studied immiscible layered two-phase flow between two parallel plates. In the simulation, as illustrated in Fig. 3, the periodic boundary condition was applied on the left and right boundaries while the non-slip (bounce-back)

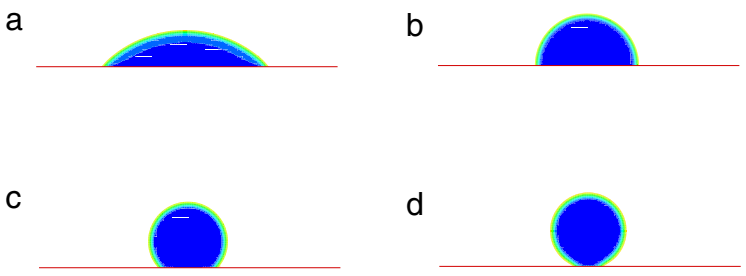

Fig. 2. Different contact angles obtained through adjusting the parameter ω in the FE model. The computational domain is 200×100 lu^2. The relaxation parameters for the blue (gray) and white phases are $\tau_1 = 0.6$, $\tau_2 = 1.0$, respectively. The $\tilde{\omega}$ and θ are (a) $\tilde{\omega} = -0.4733$, $\theta = 45°$, (b) $\tilde{\omega} = 0$, $\theta = 90°$, (c) $\tilde{\omega} = 0.4733$, $\theta = 135°$, (d) $\tilde{\omega} = 0.68$, $\theta = 176°$. (For interpretation of the references to colour in this figure legend, the reader is referred to the web version of this article.)

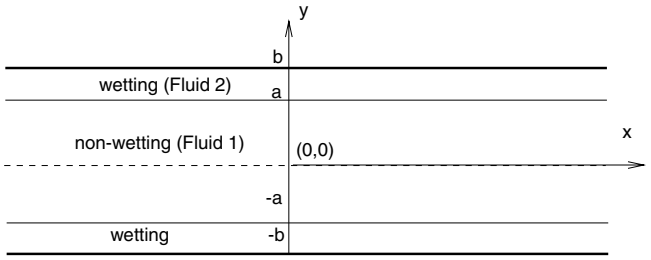

Fig. 3. Layered immiscible two-phase flow in a 2D channel. The wetting (fluid 2) phase flows along the upper and lower plate while the nonwetting phase (fluid 1) flows in the center region.

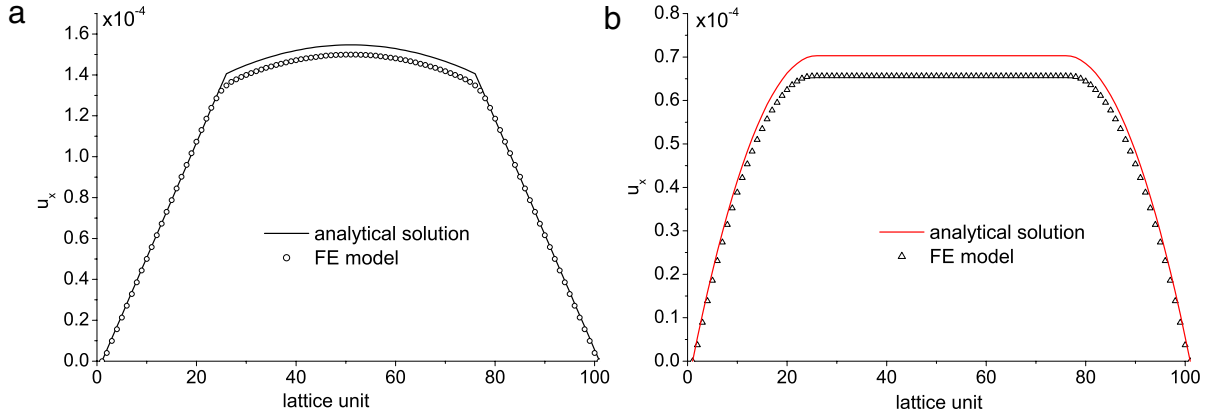

Fig. 4. Velocity profile comparison for a case of $M = 5$, $G = 1.5 \times 10^{-8}$, $S_w = 0.5$, $\tau_{nw} = 1.5$, and $\tau_w = 0.7$, when the body force G is only applied to fluid 1 (a) and fluid 2 (b).

boundary condition was applied on the upper and lower plates. The kinematic viscosities for nonwetting and wetting fluid are $\nu_{nw} = c_s^2(\tau_{nw} - 0.5)$ and $\nu_w = c_s^2(\tau_w - 0.5)$, respectively.

In the simulation, the nonwetting phase flows in the central region $0 < |y| < a$, while the wetting phase flows in the region $a < |y| < b$. Obviously, the saturation of wetting fluid in this study is $S_w = 1 - \frac{a}{b}$, and $S_{nw} = \frac{a}{b}$. Assuming a Poiseuille-type flow in the channel, the analytical solution for the velocity profile between the parallel plates can be obtained [18,40].

In our simulations, the computational domain is 10×100. Because the periodic boundary condition is used on the left and right boundaries, the mesh used in the x direction can be much smaller.

Fig. 4 shows the velocity profile across a section of the channel at $x = 5$ for $M = 5$ and $S_w = 0.5$, which is obtained from the FE model. In the figure, velocity profiles in (a) and (b) are obtained through applying the body force $G = 1.5 \times 10^{-8}$ to fluid 1 and fluid 2, respectively. The numerical solutions agree well with the analytical solutions.

Fig. 5 shows the velocity profile for $M = 1$ and $S_w = 0.5$ that is obtained from the S–C model. The numerical result is also good but there is a small jump across the interface which is also noted in Ref. [40].

To further evaluate the S–C, R–K, and FE models, the error between numerical and analytical solutions at the final steady state is illustrated in Table 1. The error between numerical and analytical solutions is defined as $\mathrm{Err}(t) = \sum_i |u_0(y_i) -$

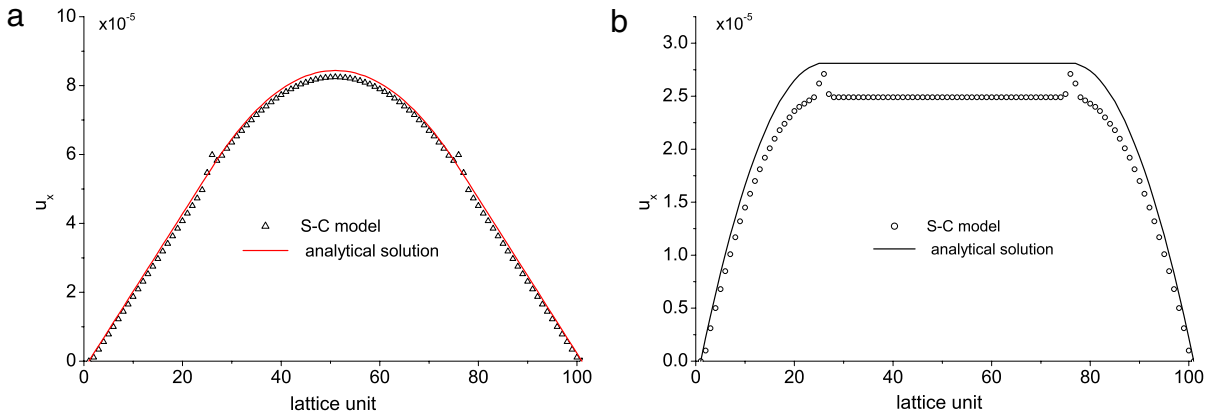

Fig. 5. Velocity profile comparison for a case of $M = 1$, $G = 1.5 \times 10^{-8}$, $S_w = 0.5$, $\tau_1 = 1.0$, and $\tau_2 = 1.0$ when the body force G is applied only to fluid 1 (a) or fluid 2 (b). The numerical solution is obtained with the S–C model.

Table 1
S–C, R–K, FE model performance in the simulation of a layered two-phase flow with different viscosity ratios.

Case		S–C	R–K	FE
$M = 1$ ($G_1 = 0, G_2 \neq 0$)	Error (%)	11.4	1.19	3.63
	ts	80,000	90,000	90,000
$M = 1$ ($G_1 \neq 0, G_2 = 0$)	Error (%)	3.07	0.585	1.62
	ts	90,000	100,000	80,000
$M = 5$ ($G_1 = 0, G_2 \neq 0$)	Error (%)	33.6	1.52	6.63
	ts	80,000	170,000	150,000
$M = 5$ ($G_1 \neq 0, G_2 = 0$)	Error (%)	33.4	3.21	2.56
	ts	80,000	170,000	160,000
$M = \frac{1}{50}$ ($G_1 = 0, G_2 \neq 0$)	Error (%)	–	1.78	2.64
	ts	–	750,000	750,000
$M = \frac{1}{50}$ ($G_1 \neq 0, G_2 = 0$)	Error (%)	–	15.58	11.13
	ts	–	630,000	670,000

$u(y_i, t)|$, where the summation is over the lattice nodes y_i in the slice $x = 5$, and u_0 is the analytical solution. The convergence criterion is $\left|\frac{\mathrm{Err}(t)-\mathrm{Err}(t-10\,000)}{\mathrm{Err}(t-10\,000)}\right| < 0.0001$.

In the table, G_1 and G_2 mean the body forces applied to component 1 and 2, respectively. For the cases with $M = 1$, the relaxation times are $\tau_1 = 1$ and $\tau_2 = 1$ in all models. For the cases with $M = 5$, the relaxation times are $\tau_1 = 1.5$ and $\tau_2 = 0.7$ in the R–K model and FE model. For the S–C model, it is difficult to achieve a specified viscosity ratio. That will be illustrated in detail in the following section. For the cases with $M = \frac{1}{50}$, the relaxation times are $\tau_1 = 0.51$ and $\tau_2 = 1.0$ in the R–K model and the FE model, and the S–C two-component model does not work for these parameters. From the table we can see that in some cases, the error of the S–C model is much larger than those of the R–K and the FE models, while the errors of the R–K and FE models are small and of the same order.

The time steps required for the velocities to converge for cases of $M = 1$, $M = 5$, and $M = \frac{1}{50}$ are also listed in Table 1. It is found for the time steps that there are very small discrepancies between the R–K model and the FE model. Because the CPU times per time step for the R–K model and the FE model are almost identical, the efficiency of the FE model is comparable to that of the R–K model.

In the S–C model, it is not easy to obtain an exact viscosity ratio other than unity because the kinematic viscosity ratio and the density ratio cannot change independently in the model [16]. For a specific G_c and equal τ values for two components, the ratio of the main fluid density to the dissolved density in the whole computational domain (except the interface area) is a constant [7].

However, if the kinematic viscosities of the two components are different, the situation is different. We carried out a series of 2D simulations where we placed a pure bubble of fluid 1 ($\rho_1 = 1.0$, $\tau_1 = 1.8$) inside a 100×100 square of fluid 2 ($\rho_1 = 0$, $\tau_2 = 0.825$) with periodic boundaries; the two fluids had equal total masses (i.e., the number of pixels occupied by fluid 1 was equal to that for fluid 2). The simulation series had initial densities of $\rho = \rho_1 + \rho_2 = 1.0$ in the whole domain and the parameter $G_c = 1.8$. It is found that the equilibrium main fluid (component 1) density and the dissolved (component 2) density inside the bubble are 1.259 and 0.009, respectively. Outside the bubble, the main fluid (component 2) density and the dissolved (component 1) density are 0.910 and 0.153, respectively. Hence, the actual viscosity

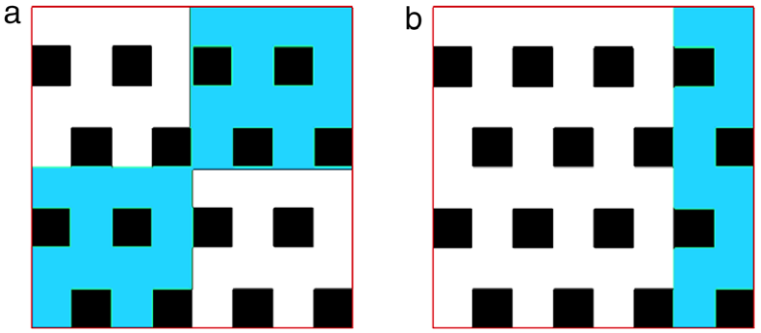

Fig. 6. Porous media and the initial phase distribution for the neutrally wetting case with $S_w = 0.5$ (a), and a fully wetting case $S_w = 0.75$ (b).

Table 2
Major parameters used in the S–C, R–K, FE models for simulation of a 160 × 160 porous medium.

Model	S–C	R–K	FE
τ_1	1.8	1.0	1.0
τ_2	0.825	0.6	0.6
σ	0.153	0.00049	0.0005
Other parameters	$G_c = 1.8$	$A = 0.00001$ $\beta = 0.5$	$\Gamma = 100$ $\tau_\phi = 0.7$ $W = 4$
Neutrally wetting case	$G_{ads1} = 0$ $G_{ads2} = 0$	$\rho_{1w} = 0$ $\rho_{2w} = 0$	$\omega = 0$
Fully wetting case (Phase 1 is nonwetting)	$G_{ads1} = 0.45$ $G_{ads2} = -0.45$	$\rho_{1w} = 0$ $\rho_{2w} = -1$	$\omega = -\sigma * 0.5105$

ratio is $M = \frac{\rho_1 c_s^2(\tau_1 - 0.5)}{\rho_2 c_s^2(\tau_2 - 0.5)} = \frac{1.259 \times (1.8-0.5)/3}{0.910 \times (0.825-0.5)/3} = 5.6$ if the more viscous component is nonwetting. Thus in this paper, for the $M = 5$ cases, the viscosity ratio in S–C model is actually $M = 5.6$ because getting the exact $M = 5$ is too difficult.

3.3. Two-phase flow in porous media

The relative permeability in porous media may be determined by the porous structure, initial wetting–saturation distribution, wettability of the porous medium, and driving force (capillary number) [11]. To minimize the effect of the porous structure, a homogeneous porous medium as shown in Fig. 6 is used for simulation. The size of the whole network is 160 × 160 lu^2. The porosity of the network is $\epsilon = 0.75$. For all of the cases in this section, $Ca = \frac{G}{\sigma(\delta x)} = 10^{-3}$, where G is the body force applied to a fluid. The initial phase distribution may affect the final distribution and hence the relative permeabilities [11].

In this section we simulated a neutrally wetting case with $S_w = 0.5$ and a fully wetting case with $S_w = 0.75$. The initial phase distributions for the neutrally wetting case and the fully wetting case are shown in Fig. 6(a) and (b), respectively.

Three nondimensional parameters are important for the immiscible two-phase flow through porous media. These parameters are the Reynolds number $Re = ud/\nu$, viscosity ratio M, and capillary number Ca. d is the width of the smallest channel in a porous medium. The maximum velocity in our simulations is 0.02 lu/ts; hence, the Reynolds number is kept very small to satisfy Darcy's law. In all of the simulations, the viscosity ratio of the two components is 5.

In the simulations, periodic boundary conditions were applied in all directions. The major parameters in our simulations are listed in Table 2. In the table, ρ_{1w} and ρ_{2w} in the R–K model mean the densities of components 1 and 2 at the wall nodes. The spurious velocity magnitudes of these cases in the S–C, R–K, and FE models are 0.02, 0.0002, and 8×10^{-6}, respectively.

The steady-state distributions of the two fluids in the porous medium of Fig. 6 obtained from the FE model and the R–K model are shown in Fig. 7(a) and (b). The velocity vectors are also shown in the figure. In the figure, both the wetting and nonwetting phases are continuous. The final distributions obtained from the FE model and the R–K model agree very well. However, the spurious velocity near the interface in Fig. 7(b) is larger than that in Fig. 7(a). In terms of the spurious velocity, the FE model is able to give a better result than the R–K model when $Ca = 10^{-3}$.

In the fully wetting case, the contact angle of fluid 2 is 0° (wetting) and the contact angle of fluid 1 is 180°, which is totally nonwetting. In these fully wetting cases, countercurrent steady-state distribution patterns obtained from the FE and the R–K models with $S_w = 0.75$ are illustrated in Fig. 8. In the figure, the FE model also demonstrates much smaller spurious velocity when $Ca = 10^{-3}$.

The wetting and nonwetting phase flow fluxes were also calculated at the bottom boundary during the simulations. A typical co-current flow flux variation as a function of the time steps is illustrated in Fig. 9. In this neutrally wetting case, the

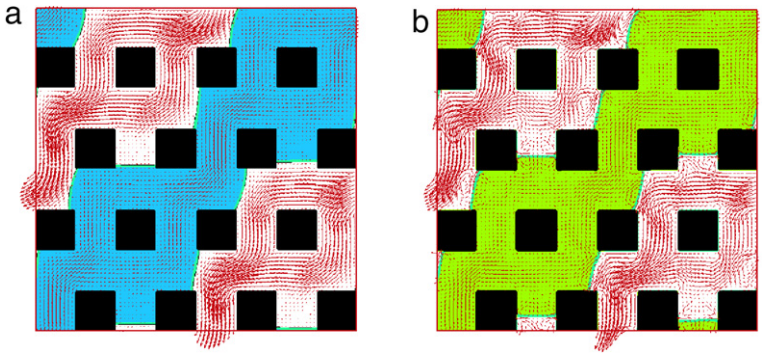

Fig. 7. Countercurrent final steady-state two-fluid distribution pattern in the case of $S_w = 0.5$, where the less viscous fluid (fluid 2) is white and the solid is black. In the LBM simulations, $\tau_1 = 1.0$, $\tau_2 = 0.6$, and $Ca = 10^{-3}$; (a) obtained from the FE model; (b) obtained from the R–K model.

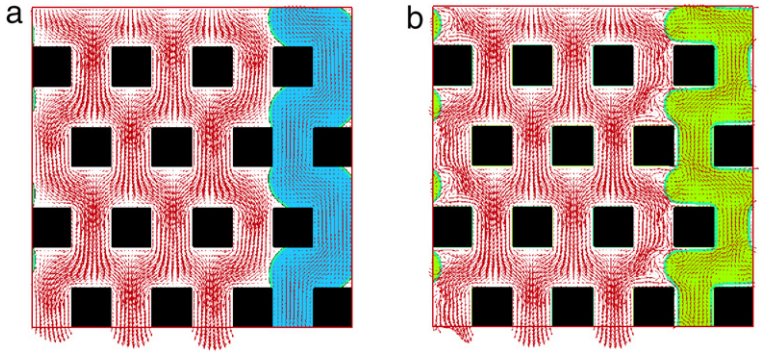

Fig. 8. The final steady-state two-fluid distribution pattern in a fully wetting countercurrent flow. The nonwetting fluid (fluid 1) is gray and the solid is black. In the LBM simulations, $\tau_{nw} = 1.0$, $\tau_w = 0.6$, and $Ca = 10^{-3}$; (a) obtained from the FE model; (b) obtained from the R–K model.

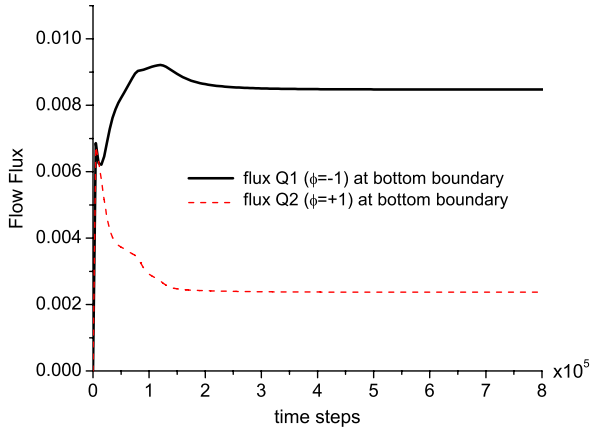

Fig. 9. A typical flow flux variation as a function of the time steps; neutrally wetting FE simulation.

FE model is used and the fluid component with $\phi = -1$ is less viscous with $\tau = 0.6$. From the figure we can see that the initialization is not far from the final steady state, and that around 5×10^5 time steps were required to converge to a steady state.

The relative permeabilities can be obtained as

$$k_w = \frac{Q_w}{Q_{w0}}, \qquad k_{nw} = \frac{Q_{nw}}{Q_{nw0}}, \tag{25}$$

where Q_w and Q_{nw} mean the flow fluxes of the wetting phase and nonwetting phase in the two-phase flow, respectively. Q_{w0} and Q_{nw0} mean the flow fluxes of wetting and nonwetting phases, respectively, when the channel is filled with only one fluid.

Table 3
Relative permeability of the co-current and countercurrent two-phase flow in a porous medium (neutrally wetting cases, $S_w = 0.5$).

Model	Co-current		Countercurrent	
	$k1$ (more viscous)	$k2$	$k1$	$k2$
S–C	0.119	0.140	−0.171	0.134
R–K	0.324	0.251	−0.253	0.191
FE	0.313	0.219	−0.273	0.221

Table 4
Relative permeability of the co-current and countercurrent two-phase flow in a porous medium ($S_w = 0.75$).

Model	Co-current		Countercurrent	
	$k1$ (more viscous)	$k2$	$k1$	$k2$
S–C	0.213	0.455	−0.186	0.462
R–K	0.252	0.683	−0.247	0.688
FE	0.290	0.740	−0.273	0.722

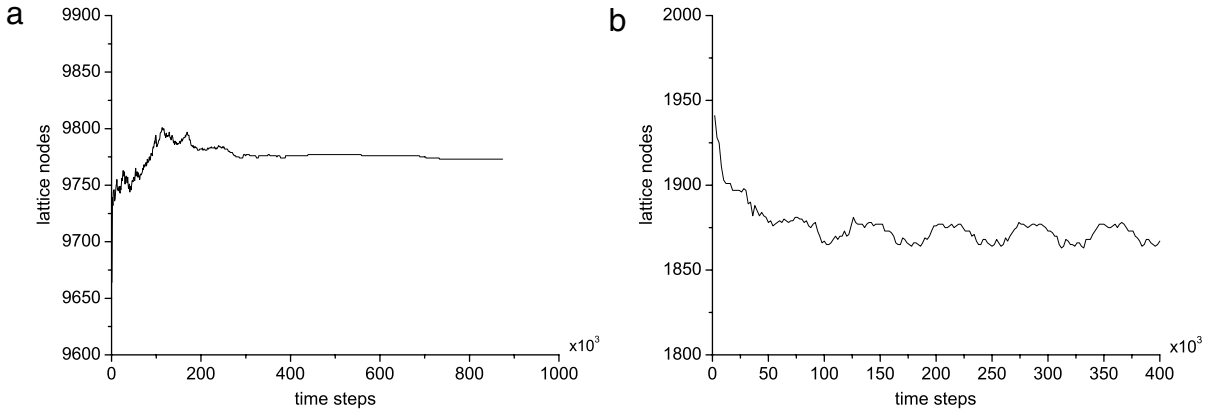

Fig. 10. The lattice nodes occupied by $\phi < 0$ component in the domain when the FE model is used. (a) A neutrally wetting countercurrent flow. In the simulation, $\tau_{nw} = 1.0$, $\tau_w = 0.6$, and $Ca = 10^{-3}$. (b) The Galilean invariance test.

For single-phase flow, the permeability of the porous medium is slightly dependent on τ when the BGK model is used for the collision term [11]. For example, when $\tau = 0.6, 0.8, 1.0$, and 1.8, the permeabilities of the porous medium are $k = 16.51$, 17.30, 17.58, and 18.74 lu^2, respectively. Hence Q_{nw0} and Q_{w0} can be calculated at a specific τ and G.

In Tables 3 and 4, the relative permeabilities for the co-current flow and countercurrent flow are listed. The relative permeabilities were obtained by using Eq. (25), i.e., the nonwetting and wetting fluid flow are divided by the corresponding Q_{nw0} and Q_{w0}. From Tables 3 and 4, we can see that the results from the FE model and the R–K model agree well. The performance of the FE model seems as good as that of the R–K model. We also found that there is a large discrepancy between the results from the S–C model and the other models.

We also compared the CPU time for 10,000 time steps when the S–C, the R–K, and the FE models were used to simulate the flow in the 160 × 160 porous medium. The CPU times for 10,000 time steps in the S–C, R–K, and FE models are 546 s, 692 s, and 606 s, respectively. Because the numbers of time steps required for convergence are similar for the R–K and FE models, we can see that the efficiency of the FE model is as good as that of the R–K model.

There is also an important concern about the mass conservation property of the FE model. Fig. 10 illustrates the lattice nodes occupied by the $\phi < 0$ component as a function of time. In the case of a neutrally wetting countercurrent flow (subfigure (a)), simulated for 900 thousand time steps, the mass of the $\phi < 0$ component almost becomes a constant. We can also see that there is a very small change from the initial value. In the subfigure (b), we can see that after 100 thousand time steps, the mass of the $\phi < 0$ component (mass inside the bubble) appears to be oscillating around a constant with small amplitude. From the figure, we can see that the FE model's mass conservation property is very good.

4. Conclusions

Here a multiphase lattice Boltzmann method based on the free energy was evaluated and compared with the performance of the S–C and R–K models. This FE model is found to satisfy the Galilean invariance through a numerical test. It is able to simulate multiphase flows with large viscosity ratio accurately—it is comparable to the R–K model. In terms of efficiency, the FE model is also as good as the R–K model. The FE model is found able to mimic multiphase flow in the model porous

medium with very small spurious velocity as compared with the main velocity of the fluids at $Ca = 10^{-3}$. The FE model is expected to be applicable for investigating 3D multiphase flow in complex heterogeneous porous media in future study.

Acknowledgements

The authors thank the anonymous referees for comments and suggestions which led to great improvement of the quality of the paper. We are grateful to Dr. Michael Sukop for his good suggestions and helpful comments. We also acknowledge discussions with Dr. Juejie Huang. This work was supported by the National Science Foundation of China (NSFC, No: 10802085), the Innovation Project of the Chinese Academy of Sciences (Grant No. KJCX2-YW-21), and the Fundamental Research Funds for the Central Universities.

References

[1] L.-S. Luo, Unified theory of the lattice Boltzmann models for nonideal gases, Phys. Rev. Lett. 81 (8) (1998) 1618–1621.
[2] T. Inamuro, T. Ogata, S. Tajima, N. Konishi, A lattice Boltzmann method for incompressible two-phase flows with large density differences, J. Comput. Phys. 198 (2) (2004) 628–644.
[3] X. Shan, G. Doolen, Multicomponent lattice-Boltzmann model with interparticle interaction, J. Stat. Phys. 81 (1995) 379–393.
[4] M.C. Sukop, D.T. Thorne, Lattice Boltzmann Modeling: An Introduction for Geoscientists and Engineers, 1st ed., Springer, Heidelberg, Berlin, New York, 2006.
[5] Q.J. Kang, D.X. Zhang, S.Y. Chen, Displacement of a two-dimensional immiscible droplet in a channel, Phys. Fluids 14 (9) (2002) 3203–3214.
[6] R. Benzi, L. Biferale, M. Sbragaglia, S. Succi, F. Toschi, Mesoscopic modeling of a two-phase flow in the presence of boundaries: the contact angle, Phys. Rev. E 74 (2) (2006) 021509.
[7] H.B. Huang, D.T. Thorne, M.G. Schaap, M.C. Sukop, Proposed approximation for contact angles in Shan-and-Chen-type multicomponent multiphase lattice Boltzmann models, Phys. Rev. E 76 (2007) 066701.
[8] M. Latva-Kokko, D.H. Rothman, Static contact angle in lattice Boltzmann models of immiscible fluids, Phys. Rev. E 72 (4) (2005) 046701.
[9] A.D. Angelopoulos, V.N. Paunov, V.N. Burganos, A.C. Payatakes, Lattice Boltzmann simulation of nonideal vapor–liquid flow in porous media, Phys. Rev. E 57 (3) (1998) 3237–3245.
[10] C. Pan, M. Hilpert, C.T. Miller, Lattice-Boltzmann simulation of two-phase flow in porous media, Water Resour. Res. 40 (2004) W01501.
[11] H. Li, C. Pan, C.T. Miller, Pore-scale investigation of viscous coupling effects for two-phase flow in porous media, Phys. Rev. E 72 (2005) 026705.
[12] K. Langaas, P. Papatzacos, Numerical investigations of the steady state relative permeability of a simplified porous medium, Transp. Porous Media 45 (2001) 241–266.
[13] A.K. Gunstensen, D.H. Rothman, S. Zaleski, G. Zanetti, Lattice Boltzmann model of immiscible fluids, Phys. Rev. A 43 (8) (1991) 4320–4327.
[14] D.H. Rothman, J.M. Keller, Immiscible cellular-automaton fluids, J. Stat. Phys. 52 (3–4) (1988) 1119–1127.
[15] D. Grunau, S. Chen, K. Eggert, A lattice Boltzmann model for multiphase fluid flows, Phys. Fluids A 5 (10) (1993) 2557–2562.
[16] B. Ahrenholz, J. Tolke, P. Lehmann, A. Peters, A. Kaestner, M. Krafczyk, W. Durner, Prediction of capillary hysteresis in a porous material using lattice Boltzmann methods and comparison to experimental data and a morphological pore network model, Adv. Water Resour. 31 (9) (2008) 1151–1173.
[17] X. Shan, H. Chen, Lattice Boltzmann model for simulating flows with multiple phases and components, Phys. Rev. E 47 (3) (1993) 1815–1819.
[18] H.B. Huang, X.-Y. Lu, Relative permeabilities and coupling effects in steady-state gas–liquid flow in porous media: a lattice Boltzmann study, Phys. Fluids 21 (9) (2009) 092104.
[19] M.R. Swift, W.R. Osborn, J.M. Yeomans, Lattice Boltzmann simulation of nonideal fluids, Phys. Rev. Lett. 75 (5) (1995) 830–833.
[20] H.W. Zheng, C. Shu, Y.T. Chew, A lattice Boltzmann model for multiphase flows with large density ratio, J. Comput. Phys. 218 (2006) 353–371.
[21] S.L. Hou, X.W. Shan, Q.S. Zou, et al., Evaluation of two lattice Boltzmann models for multiphase flows, J. Comput. Phys. 138 (2) (1997) 695–713.
[22] X.Y. He, S.Y. Chen, R.Y. Zhang, A lattice Boltzmann scheme for incompressible multiphase flow and its application in simulation of Rayleigh–Taylor instability, J. Comput. Phys. 152 (2) (1999) 642–663.
[23] T. Lee, C.L. Lin, A stable discretization of the lattice Boltzmann equation for simulation of incompressible two-phase flows at high density ratio, J. Comput. Phys. 206 (2005) 16–47.
[24] A. Fakhari, M.H. Rahimian, Phase-field modeling by the method of lattice Boltzmann equations, Phys. Rev. E 81 (2010) 036707.
[25] O.R. Ayodele, Theoretical analysis of viscous coupling in two-phase flow through porous media, Transp. Porous Media 64 (2006) 171–184.
[26] F. Kalaydjian, Origin and quantification of coupling between relative permeabilities for 2-phase flows in porous-media, Transp. Porous Media 5 (1990) 215–229.
[27] N.S. Martys, H.D. Chen, Simulation of multicomponent fluids in complex three-dimensional geometries by the lattice Boltzmann method, Phys. Rev. E 53 (1) (1996) 743–750.
[28] M.C. Sukop, H.B. Huang, C.L. Lin, M.D. Deo, K. Oh, J.D. Miller, Distribution of multiphase fluids in porous media: Comparison between lattice Boltzmann modeling and micro-x-ray tomography, Phys. Rev. E 77 (2008) 026710.
[29] D. Jacqmin, Calculation of two-phase Navier–Stokes flows using phase-field modeling, J. Comput. Phys. 155 (1999) 96–127.
[30] V.M. Kendon, M.E. Cates, I. Pagonabarraga, J.C. Desplat, P. Bladon, Inertial effects in three-dimensional spinodal decomposition of a symmetric binary fluid mixture: a lattice Boltzmann study, J. Fluid Mech. 440 (2001) 147–203.
[31] N. Takada, M. Misawa, A. Tomiyama, S. Hosokawa, Simulation of bubble motion under gravity by lattice Boltzmann method, J. Nucl. Sci. Technol. 38 (5) (2001) 330–341.
[32] J.J. Huang, C. Shu, Y.T. Chew, Mobility-dependent bifurcations in capillarity-driven two-phase fluid systems by using a lattice Boltzmann phase-field model, Internat. J. Numer. Methods Fluids 60 (2009) 203–225.
[33] K. Langaas, J.M. Yeomans, Lattice Boltzmann simulation of a binary fluid with different phase viscosities and its application to fingering in two dimensions, Eur. Phys. J. B 15 (1) (2000) 133–141.
[34] A. Lamura, S. Succi S, A lattice Boltzmann for disordered fluids, Internat. J. Modern Phys. B 17 (2003) 145–148.
[35] M.R. Swift, E. Orlandini, W.R. Osborn, J.M. Yeomans, Lattice Boltzmann simulations of liquid–gas and binary fluid systems, Phys. Rev. E 54 (5) (1996) 5041–5052.
[36] D. Jamet, D. Torres, J.U. Brackbill, On the theory and computation of surface tension: the elimination of parasitic currents through energy conservation in the second-gradient method, J. Comput. Phys. 182 (2002) 262–276.
[37] J.S. Rowlinson, B. Widom, Molecular Theory of Capillarity, Clarendon, Oxford, 1989.
[38] T. Inamuro, N. Konishi, F. Ogino, Galilean invariant model of the lattice Boltzmann method for multiphase fluid flows using free-energy approach, Comput. Phys. Comm. 129 (2000) 32–45.
[39] A.J. Briant, J.M. Yeomans, Lattice Boltzmann simulations of contact line motion. II. Binary fluids, Phys. Rev. E 69 (2004) 031603.
[40] Q.J. Kang, D.X. Zhang, S. Chen, Immiscible displacement in a channel: simulations of fingering in two dimensions, Adv. Water Resour. 27 (2004) 13–22.